ARTICLE

**OPEN**

Check for updates

# Electron localization induced by intrinsic anion disorder in a transition metal oxynitride

Daichi Oka [1,2✉], Yasushi Hirose [2,3], Shoichiro Nakao[2,3], Tomoteru Fukumura[1,4] & Tetsuya Hasegawa[2,3]

Anderson localization derived from randomness plays a crucial role in various kinds of phase transitions. Although treated as a free variable parameter in theory, randomness in electronic materials is hard to control experimentally owing to the coexisting Coulomb interaction. Here we demonstrate that the intrinsic anion disorder in a mixed-anion system of $SrNbO_2N$ induces a significant random potential that overwhelms the Coulomb potential while maintaining the lattice structure. A metal-to-insulator transition is triggered by a chemical modulation of the electron density where the critical electron density is more than three orders of magnitude greater than that predicted by the well-known Mott criterion. The localized electrons show characteristic electrical properties such as temperature-dependent multiple crossovers of conduction mechanisms and a positive magnetoresistance above 50% at low temperature. The large magnetoresistance is attributed to wave-function shrinkage of the localized states and clearly visualizes the anisotropy in the band structure, which indicates a compatibility of the periodicity and randomness.

[1] Department of Chemistry, Graduate School of Science, Tohoku University, 6-3 Aramaki Aza Aoba, Aoba, Sendai, Miyagi 980-8578, Japan. [2] Department of Chemistry, School of Science, The University of Tokyo, 7-3-1 Hongo, Bunkyo, Tokyo 113-0033, Japan. [3] Kanagawa Academy of Science and Technology (KAST), 3-2-1 Sakado, Takatsu, Kawasaki 213-0012, Japan. [4] Advanced Institute for Materials Research, Tohoku University, 2-1-1 Katahira, Sendai, Miyagi 980-8577, Japan. ✉email: daichi.oka.d2@tohoku.ac.jp

A doped semiconductor shows a divergence of the electrical resistivity toward absolute zero temperature when the Fermi energy is less than a threshold known as the mobility edge. The origin of the insulating behaviour, despite the existence of electrical carriers, was successfully explained as a result of carrier localization by the random potential generally formed by the disorder of the dopants or defects, which was initially proposed by Anderson[1–4]. After more than 50 years of investigations to understand the localization and delocalization phenomena, Anderson localization theory has been extended to various phase transitions in addition to the simple metal-insulator transition (MIT) in semiconductors. A typical example of an Anderson transition is the steep change of resistivity observed in quantum Hall effects of two-dimensional systems[3,4]. Recent studies showed that disorder can stabilize not only insulating states but also functional phases such as superconductors[5,6] and topologically non-trivial states[7–9]. It was also found that the ferromagnetism in diluted magnetic semiconductors is mediated by localized electrical carriers[10,11].

One of the focuses in the theoretical studies on Anderson localization is phase control using disorder as a variable, which has been in part realized experimentally for non-interacting waves such as ultracold atoms and light[8,9]. However, it is still challenging to control the electronic phase of materials by using a random potential owing to the presence of the Coulomb interaction, which is another possible origin for MIT as proposed by Mott[12]. In both systems dominated by disorder and a Coulomb interaction, MIT occurs at a critical carrier concentration $n_c$ by varying the carrier concentration $n$. Although random and Coulomb potentials coexist in actual doped semiconductors, MITs are generally triggered by the latter, which follows the Mott criterion $n_c^{1/3}a_0 = 0.26$, where $a_0$ is the effective Bohr radius in the non-doped state[13].

It is essential to introduce significant randomness that can overwhelm the Coulomb interaction to achieve a disorder-induced Anderson insulator. Recently, polycrystalline thin films of a phase-change material $GeSb_2Te_4$ with the significant structural disorder were reported to show a disorder-induced MIT at an $n_c$ that was orders of magnitude higher than that expected by the Mott criterion[14]. This implies that a large number of electrical carriers were localized compared with other materials. Later, a similar disorder-induced MIT was observed in single crystals of Li doped $Fe_7Se_8$[15]. In these materials, the strong disorder originated not from dopants but the cation vacancies, thus $n$ was modulated without significant change in the random potential. However, such a strategy for introducing significant randomness requires robustness of the crystalline framework against local strain and thus is not widely applicable to other systems. Additionally, significant local lattice deformations caused by randomly distributed vacancies would change the band structure significantly, making it difficult to understand the physical properties based on the band theory. Thus, a route to introduce a strong electronic disorder to a crystal without significant lattice deformation is required to understand localization phenomena from a microscopic point of view and to apply them to phase control.

In this study, we report on Anderson localization of electrons induced by an intrinsic disorder of anions in epitaxial thin films of a mixed-anion system of $SrNbO_2N$. $SrNbO_2N$ is a perovskite-type oxynitride semiconductor with a simple band structure and preferably forms a complicated chain-like bonding network of Nb and $X$ anions ($X = O^{2-}$ and $N^{3-}$) as shown in Fig. 1a[16,17], which leads to significant random potential in the $-X-B-X-$ electrical pathway. It should be noted that both $X$ anions are expected to contribute to the electrical conduction almost equally considering the similar hybridizations between the Nb 4d and O/N 2p orbitals[18], maintaining the electrical conduction
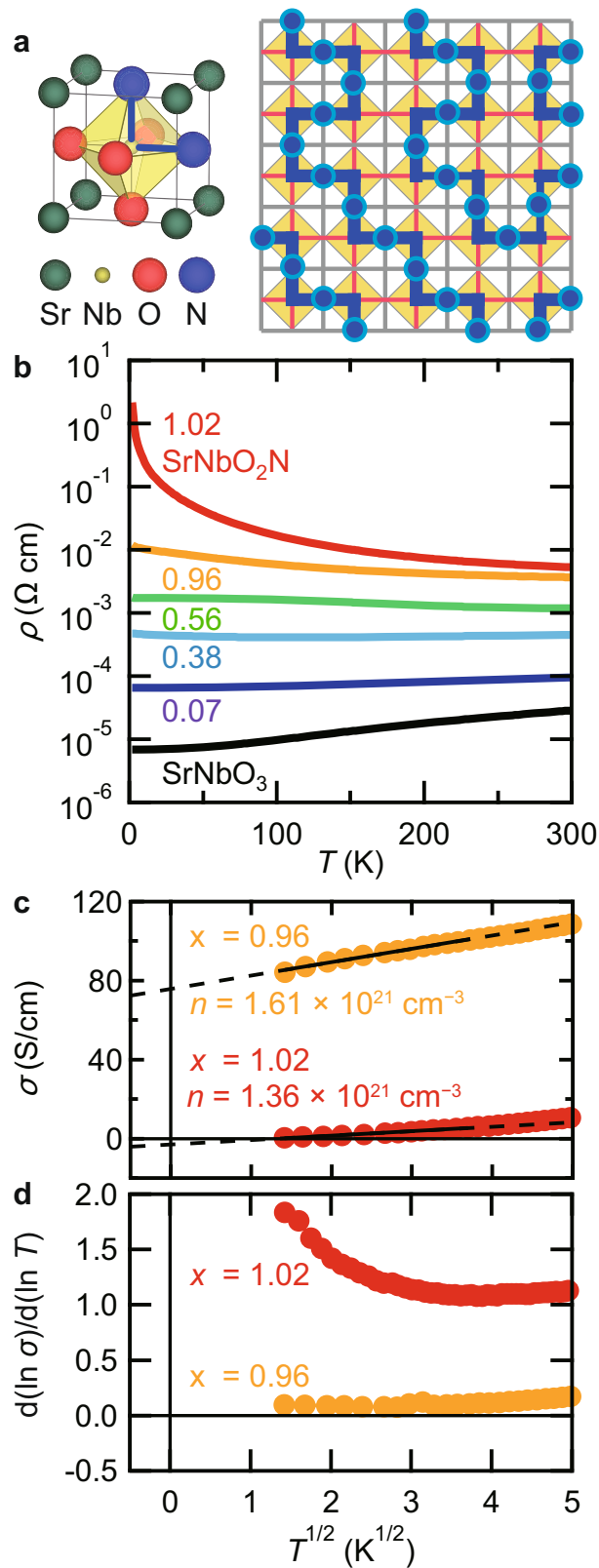


three-dimensional. We demonstrate disorder-induced MIT triggered by a slight modulation of $n$ through the anion composition without significant change in the crystal structure, where $n_c$ is three orders of magnitude higher than that expected from the Mott criterion. A small Coulomb gap totally encapsulated in the localized state originated temperature-dependent multiple crossovers in the conduction mechanisms. Meanwhile,

**Fig. 1 Metal-to-insulator transition (MIT) in SrNbO$_{3-x}$N$_x$. a** Crystal structure of *cis*-type perovskite SrNbO$_2$N and a schematic image of the cross-sectional (100) plane with a chain-like anion network in SrNbO$_2$N. **b** Temperature $T$ dependence of resistivity $\rho$ for SrNbO$_{3-x}$N$_x$ epitaxial thin films. **c** Conductivity $\sigma$ and **d** d(ln $\sigma$)/d(ln $T$) as functions of $T^{1/2}$ for the SrNbO$_{3-x}$N$_x$ epitaxial thin films with $x = 0.96$ and 1.02. The relative standard deviations for the vertical axes determined by 10 times measurements were within 0.3% and 7% for $x = 0.96$ and 1.02, respectively, in **c** and **d**, which were negligibly small in the analyses of MIT.

the survival of the periodicity of the perovskite lattice structure was indicated by the anisotropic large magnetoresistance.

## Results and discussion

**Metal-insulator transition in SrNbO$_{3-x}$N$_x$ films.** We investigated SrNbO$_2$N in the form of an epitaxial thin film, which was beneficial for the suppression of extrinsic disorders, such as grain boundaries, and an accurate examination of the electrical conduction and crystallographic anisotropy. For comparison, SrNbO$_{3-x}$N$_x$ ($0 \le x \le 1.02$) (001) epitaxial thin films with various nitrogen contents $x$ were grown on KTaO$_3$ (001) single crystals with nitrogen-plasma-assisted pulsed laser deposition[18–24]. An almost ideal nitrogen content $x$ of 1.02 was observed for the SrNbO$_2$N epitaxial thin film. Epitaxial growth on the KTaO$_3$ (001) substrates with a cube-on-cube manner was confirmed by spot X-ray diffraction peaks of both symmetric 002 and asymmetric 101 diffractions in two-dimensional detector images for all the films (Supplementary Figs. 1 and 2). Reciprocal space mapping for the SrNbO$_2$N thin film also showed a spot 103 diffraction peak (Supplementary Fig. 3). Unlike the coherently grown SrNbO$_3$[25], the SrNbO$_2$N thin film showed partial relaxation from the substrate, resulting in lattice constants of $a = 4.03$ Å and $c = 4.06$ Å and a tetragonal distortion of $c/a = 1.007$. Flat surfaces with root mean square roughness less than 1 nm were observed by atomic force microscope (Supplementary Fig. 4). The detail of the crystal growth and the room-temperature properties of the films have been reported elsewhere[18,25,26].

First, we observed the effect of nitrogen substitution on the electrical conductivity in SrNbO$_{3-x}$N$_x$ from the temperature $T$ dependence of the resistivity $\rho$ (Fig. 1b). Reflecting the change of the band filling from the 4d$^1$ metallic state of SrNbO$_3$ ($x = 0$) to the 4d$^0$ semiconducting state of SrNbO$_2$N ($x = 1$), $\rho$ and its differential d$\rho$/d$T$ decreased with increasing $x$, where the carrier polarity was always $n$-type. The sign of d$\rho$/d$T$ was changed from positive to negative at the boundary composition of $x = 0.38$, whose $\rho$ value of 451 μΩ cm at 300 K well corresponded to the saturation resistivity of 500 μΩ cm at the phenomenological Mott-Ioffe-Regel (MIR) limit[27,28]. Indeed, the MIR limit lied between $x = 0.38$ and 0.55 by using the criterion $k_F l_e \approx \pi$, where $k_F$ is the Fermi wave number and $l_e$ is the electron mean free path (see Supplementary Note 1 for detail)[29]. The film thickness and the grain size were much larger than $l_e$ for all the films (Supplementary Table 1), confirming that the composition-dependent change of electrical conductivity was not induced by extrinsic electron scattering. The systematic composition dependence of the electrical conductivity without any sign of dimensionality change indicated that the electrical pathway was maintained three-dimensional from SrNbO$_3$ to SrNbO$_2$N. In stark contrast with the gradual change in $\rho$ and d$\rho$/d$T$ by variation of the composition from $x = 0$ to 0.96, a divergence behaviour toward 0 K suddenly emerged at $x = 1.02$, which indicated MIT between $x = 0.96$ and 1.02. In the composition range from $x = 0$ to $x = 0.56$, the carrier density $n$ corresponded to the number of 4d electrons[18]. Meanwhile, $n$ of the thin films with $x = 0.96$ and 1.02 was around $1 \times 10^{21}$ cm$^{-3}$, which was much higher than the value expected from the nominal Nb valence. This indicated electron doping by the corresponding number of oxygen vacancies. Considering the nitrogen density of

around $1.5 \times 10^{22}$ cm$^{-3}$ was one order of magnitude larger than $n$, the disorder caused by the vacancies could be ignored.

Metal and insulator phases were distinguished by positive and negative slopes of the $\rho$–$T$ curves, respectively, in the previous reports on the disorder-induced MIT[14,15]. Nevertheless, such assignments cause significant overestimation of $n_c$, being not appropriate in the regime of Anderson localization theory constructed for ground states[30]. Instead, we confirmed MIT between $x = 0.96$ and 1.02 by examining the conductivity at absolute zero temperature with the two kinds of plots shown in Fig. 1c, d. The conductivities at absolute zero temperature, which were extrapolated from the $T^{1/2}$ dependence of conductivity $\sigma$, were positive and negative for $x = 0.96$ and $x = 1.02$, respectively (Fig. 1c). This indicated that the former was metal and the latter was an insulator in the framework of the localization theory[31]. This assignment was further confirmed by the more accurate analysis using the quantity $w = $ d(ln $\sigma$)/d(ln $T$) as a function of $T^{1/2}$ shown in Fig. 1d[32]. The positive and negative slopes at low temperatures indicated metallic and insulating conduction of the films with $x = 0.96$ and 1.02, respectively. Considering the similar degree of disorder derived from the similar density of nitrogens, the MIT was triggered by the change of $n$ in the electron-doped regime. Accordingly, $n_c$ corresponding to the mobility edge of SrNbO$_2$N was between $1.36 \times 10^{21}$ cm$^{-3}$ and $1.61 \times 10^{21}$ cm$^{-3}$.

**Band edge structure of SrNbO$_2$N film.** The band edge structure including the energetic position of the mobility edge was estimated from the thermal excitation processes of the localized electrons in the SrNbO$_2$N epitaxial thin film. Typically, $T$ dependence of $\rho$ in a localization system is formulated as follows[33,34]

$$\rho = \rho_0 \exp\left(T_0/T\right)^s \qquad (1)$$

where $\rho_0$ is the resistivity coefficient and $T_0$ is the characteristic temperature. While the Efros-Shklovskii (ES)- and Mott-variable range hopping (VRH) conduction mechanisms show the exponent $s$ of 0.5 and 0.25, respectively, the thermal activation (TA) mechanism is described by $s = 1$. Because Eq. (1) leads to the relationship $w = s(T_0/T)^s$, the exponent $s$ is experimentally determined from the slope in the ln $w$ vs. ln $T$ plot (Supplementary Fig. 5). The variation of the slope indicated crossovers of four types of conduction mechanisms as shown in Fig. 2a (see Supplementary Note 2 for detail). The exponent $s \sim 0.45$ for the region I ($T < 8$ K) corresponded to ES-VRH expressed by $\rho = \rho_0$ exp $(T_{ES}/T)^{1/2}$, implying the presence of a Coulomb gap at the Fermi level, unlike the previously reported disorder-induced Anderson insulators[14,15]. This assignment was strongly evidenced by the large magnetoresistance (MR) mentioned below. The fitting for the $\rho$-$T$ curve yielded $T_{ES} = 28.1$ K and the Coulomb gap $\Delta_C = 0.5(T_{ES}T_c)^{1/2} = 0.62$ meV (Fig. 2b), where $T_c = 8$ K is the crossover temperature from the ES-VRH to another conduction mechanism[33]. In principle, crossovers to Mott-VRH and TA behaviour are expected when the temperature is raised beyond the values corresponding to $\Delta_C$ and mobility edge, respectively, as reported for various semiconductors[35–39]. As expected, the regions III (100 K < $T$ < 160 K) and IV ($T$ > 160 K) showed $T$ dependence assignable to Mott-VRH and TA with $s = 0.25$ and 1, respectively. The energy difference between the mobility edge and the Fermi
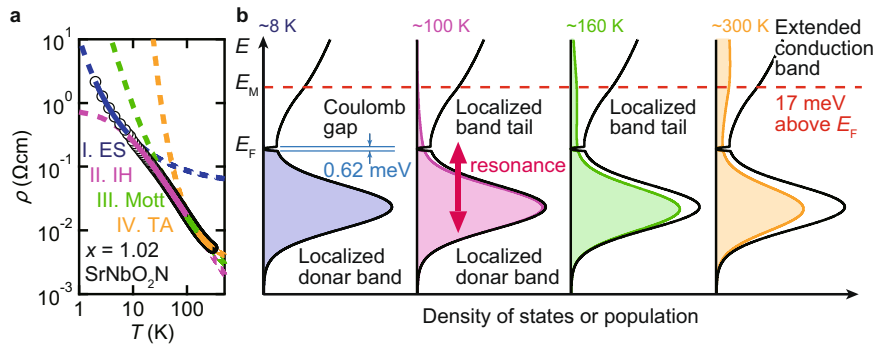
**Fig. 2 Temperature-induced crossover of electrical transport mechanisms in SrNbO$_2$N. a** Logarithmic plot of resistivity $\rho$ versus temperature $T$ for the SrNbO$_2$N epitaxial thin film with fitting results by various conduction mechanisms. ES, IH, Mott, and TA represent Efros-Shklovskii variable range hopping, inelastic hopping, Mott-variable range hopping, and thermal activation conductions, respectively. **b** Band edge structure of SrNbO$_2$N estimated from **a**. The black line and the colour shaded area represent the density of states and population at each temperature region. $E_M$ and $E_F$ represent the energy level of the mobility edge and the Fermi energy, respectively.

level was estimated to be 17 meV (197 K) from the TA behaviour in region IV (Fig. 2b). Indeed, the resistivity of the SrNbO$_2$N thin film was close to that of the SrNbO$_{3-x}$N$_x$ ($x = 0.96$) in the metallic regime with differences within 50% above 197 K (Fig. 1a), confirming that $E_F$ crossed the mobility edge lied between these two compositions.

Characteristic temperature dependence was observed in region II ($8\,\text{K} < T < 100\,\text{K}$) between the ES- and Mott-VRH for the SrNbO$_2$N thin film. Unlike the other regions, the slope in the ln $w$ vs ln $T$ plot was positive and the $T$ dependence of $\rho$ was concave up (Fig. 2a), indicating accelerating enhancement of electrical conduction with increasing $T$. Such an acceleration is assigned to inelastic hopping tunnelling conduction in resonance between distinct localized states, described by the following power law[40,41]

$$\sigma = \sigma_{\text{res}} + \sum_N C_N T^{N-2/(N+1)} \qquad (2)$$

where $\sigma_{\text{res}}$ is the residual conductivity, $C_N$ is the temperature coefficient, and $N$ is the number of multiple localized states. As in the present case, the inelastic hopping conduction often shows crossover to Mott-type VRH depending on the sample size and the localization length as a function of $n$ and $T$[40]. Assuming a power-law dependence, the $T$ exponent was analytically determined to be 1.312 for region II (Supplementary Fig. 6), which was in good agreement with the exponent of 4/3 for the hopping conduction expressed by Eq. (2) with the lowest order hopping channel ($N = 2$). Because the inelastic hopping conduction was observed in the $T$ region above that for ES-VRH, the two localized states would be attributed to the upper and lower localized bands separated by the Coulomb gap (Fig. 2b). In contrast to the nm-scale barriers in the previous reports, we observed the resonance behaviour for the mm-scale hole-bar patterned thin film. This suggested that the electrical conduction in region II was composed of a repetition of inelastic hopping processes taken place in closely similar local structures homogeneously distributed in the perovskite oxynitride, being a characteristic for the intrinsically disordered system in stark contrast to the general doped semiconductors with various local structures around the dopants.

**Investigation on the Mott criterion for SrNbO$_2$N film.** The trigger of the MIT was examined by estimating the effective Bohr radius $a_H$ of SrNbO$_2$N from MR at low temperatures close to 0 K. It should be noted that we did not use the room-temperature parameters to determine $a_H$ because they reflect the electronic states beyond the mobility edge[30]. Accompanied by the ES-VRH conduction, the SrNbO$_2$N showed large positive

magnetoresistance (MR), which increased monotonically with decreasing $T$ and reached a value of over 50% at 9 T below 2 K (Fig. 2a). The exponentially increasing MR with different slopes in the low and high magnetic field regions (Supplementary Fig. 9) was common with MR reported for semiconductors with hopping conduction[33,39,42–44], which have been explained by the wave function shrinkage (WFS) model using the following equation by means of percolation theory[33,45]

$$\text{MR}(B, T) = \exp\left\{\xi_c(0, T)\left[\xi_c(B, T)/\xi_c(0, T) - 1\right]\right\} \qquad (3)$$

where $\xi_c(B,T)$ is the percolation parameter, which was formulated especially for ES-VRH as described in Supplementary Note 3 in detail[33,45,46]. The normalized percolation parameter $\xi_c(B,T)/\xi_c(0,T)$ is a function of the normalized magnetic field $B^* = B/B_c$ with the normalization factor $B_c \equiv 6\hbar/ea_H^2(n)\xi_c(0,T)$, $\hbar$ is the Planck constant divided by $2\pi$, $e$ is the elementary charge, and $a_H(n)$ is the effective Bohr radius as a function of $n$, where $a_H(n)$ is the only free parameter. As shown in Fig. 3, the MR curves for SrNBO$_2$N at 1.3, 2, 5, and 10 K were well explained by the above equation, which indicated the validity of the WFS models and yielded an $a_H(1.36 \times 10^{21}\,\text{cm}^{-3})$ of 115(6) Å. Accordingly, the large MR is attributed to the large Bohr radius enhanced by the scaling rule described below.

We further derived $a_0 = a_H(0)$ for SrNbO$_2$N from the following equations predicted by the scaling theory

$$a_H(n) = a_0(1 - n/n_c)^{-\nu} \qquad (4)$$

with

$$a_0 = 4\pi\varepsilon(0)\varepsilon_0\hbar^2/m^* e^2 \qquad (5)$$

and

$$\varepsilon(n) = \varepsilon(0)(1 - n/n_c)^{-\zeta} \qquad (6)$$

where $\varepsilon(n)$ is the dielectric constant, $\varepsilon_0$ is the permittivity of a vacuum, $m^*$ is the electron effective mass in the clean limit without distribution of the on-site energy of electrons, and $\nu$ and $\zeta$ are the critical indices with empirically derived values of ~1/2 and ~1, respectively[47]. $\varepsilon(1.36 \times 10^{21}\,\text{cm}^{-3})$ was determined to be 145 from the relationship $T_{ES} = \beta e^2/4\pi\varepsilon(n)\varepsilon_0 a_H(n)k_B$, where $\beta$ is a numerical factor around 2.8[45], and $k_B$ is the Boltzmann constant. Considering that MIT was observed from $x = 0.96$ to 1.02 and $\varepsilon(0)$ of SrNbO$_2$N is larger than that for Sr$_2$Nb$_2$O$_7$[48,49], boundary conditions are given as $1.36 \times 10^{21}\,\text{cm}^{-3} < n_c < 1.61 \times 10^{21}\,\text{cm}^{-3}$ and $\varepsilon(0) > 10$, which yielded the possible ranges for parameters $a_0$, $\varepsilon(0)$, $m^*$, and $n_c$ from the simultaneous Eqs. (4–6) (Supplementary Table 2). $m^*$ of ca. $0.2m_0$ was close to the previous theoretical prediction[50], which supported the validity of the analysis. In
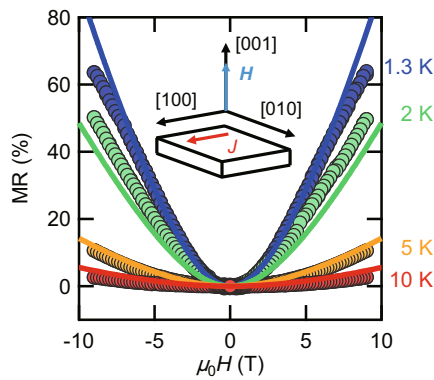
**Fig. 3 Disorder-induced magnetoresistance in SrNbO$_2$N.**
Magnetoresistance (MR) as a function of magnetic field $H$ multiplied by the vacuum permeability $\mu_0$ for the SrNbO$_2$N epitaxial thin film at various temperatures. The solid curves are the fitting results by the wave function shrinkage model. The inset shows the measurement geometry, where $I$ indicates electrical current.

addition, the electron effective mass of $0.85m_0$ previously determined by optical spectroscopy at room temperature was in the same order as $m^*$, albeit higher due to the disorder, reflecting the thermally excited electrons from the shallow donor level. $a_0 = 3.0$–$4.6$ nm led to the expectation of $n_c = 2$–$7 \times 10^{17}$ cm$^{-3}$ from the Mott criterion $n_c^{1/3}a_0 = 0.26$, which was more than three orders of magnitude lower than the observed $n_c$. This indicated that the SrNbO$_2$N was a disorder-dominated Anderson insulator (Supplementary Fig. 10). Therefore, localization of a significantly large number of electrical carriers was realized by the strong anion disorder.

**Anisotropy in the wave function of the localized electrons in SrNbO$_2$N film.** Finally, we demonstrated the survival of the band structure, which originated from the periodicity of the perovskite lattice, even in the highly disordered SrNbO$_2$N by using the anisotropy in MR. According to the WFS theory, the MR anisotropy in the real space roughly corresponds to the wave function distribution of the localized electrons in $k$-space indicated by inverse Bohr radius (see Supplementary Note 3 for detail). In a high magnetic field, $\xi_c(B,T)$ in Eq. (3) is approximated as follows[33,45,46]

$$\xi_c(B, T) = \left(T_1(B)/T\right)^{3/5} \tag{7}$$

with

$$T_1(B) = T_0 \left(\frac{ea_H^3 B}{6\hbar a_B}\right)^{1/3} \tag{8}$$

where $a_B$ is the Bohr radius in the direction parallel to field $B$. It should be noted that WFS-derived MR is independent of the current direction as observed for MR in the present SrNbO$_2$N film (Supplementary Fig. 12). We measured the anisotropy in MR for the SrNbO$_2$N epitaxial thin film in the geometry illustrated in Fig. 4a. Figure 4b, c, d shows three-dimensional plots of the angle dependence of MR at 2, 5, and 10 K in 9 T, respectively. The distributions of MR were spherical, reflecting the pseudo-cubic lattice of the perovskite structure, similar to cubic Ge[33]. The more spherical shape at lower temperatures indicated the progress of the localization effect, which generally transforms the distribution of waves to be granular and spherical even in periodic lattices[51,52]. On the other hand, the precise features clearly reflected the perovskite-type lattice structure shown in Fig. 4e. In the present SrNbO$_2$N epitaxial thin film, the out-of-plane [001] and [00$\bar{1}$] directions are not equivalent to the in-plane [100], [$\bar{1}$00], [010],

and [0$\bar{1}$0] directions due to the small tetragonal distortion of $c/a = 1.007$ induced by the epitaxial stress as mentioned above. Comparing the amplitude at the characteristic lattice directions of <001>, <100> and <110>, MR decreased in the order of <110>→ <100>→ <001>, <100>→ <001>→ <110>, and <001>→ <100>→ <110> at 2, 5, and 10 K, respectively (Fig. 4b–d, Supplementary Fig. 12). The temperature-dependent variation of the anisotropy indicated thermal excitation of the conducting electrons between bands with different symmetries against the crystallographic coordinate system. Such multiple bands were derived from the small band splitting at the bottom of the conduction band in the tetragonal geometry because the crystallographic difference between the in-plane <100> and out-of-plane <001> directions was only in the lattice constant. It should be noted that the influence of such a small strain on the anion arrangement is negligible in perovskite oxynitrides as we previously reported[23].

We investigated the distribution of the conduction band in $k$-space under the tetragonal strain by first-principles calculation. A technical issue regarding first-principles calculation on perovskite oxynitride is that the limited size of the cell requires an assumption of a certain ordered arrangement of nitrogen[18,53]. Any assumption of nitrogen ordering inevitably reduces the crystal symmetry, which causes discrepancy from the experimentally observed high-symmetry structure with the random nitrogen distribution and hinders the effect of the tetragonal distortion. That is why we used a simple model of perovskite oxide SrTiO$_3$ with the same d$^0$ configuration as SrNbO$_2$N in this study. This is a reasonable approximation because the band structure around the conduction band minimum is common for d$^0$ perovskite systems[54–56]. Figure 4f–h shows the calculated band structures without (Fig. 4h) and with (Fig. 4f, g) the tetragonal distortion of $c/a = 1.007$. While degenerate light- and heavy-mass bands were observed in the former as previously reported[55,56], the latter showed an energy level splitting. Figure 4i–k shows the constant energy surfaces of the three bands composing the bottom of the conduction band in the distorted lattice (blue, red, and green curves in Fig. 4h, respectively). While the blue and red bands were degenerate at the Γ-point, the contribution of the former to the electrical conduction is greater than that of the latter at the bottom of the conduction band because of the lighter mass of the former. Indeed, the spatial distribution of MR at 2 K (Fig. 4b) well corresponded to that of the blue band (Fig. 4i) with a square-like distribution in the $k_x$-$k_y$ plane (Fig. 4f). Because the electrons were excited more to the red band with the larger density of states (i.e. larger volume in $k$-space as shown in Fig. 4j), electrical conduction in the red band became dominant at 5 and 10 K. At 10 K, MR along the <001> direction became slightly larger than that along the <100> direction because of the additional contribution of the green band with a spatial distribution elongating to the $k_z$ axis (Fig. 4k). These good correspondences between the anisotropy in MR and the calculated band structure indicated survival of the periodic nature of the perovskite lattice even under the existence of the strong disorder of the anions.

## Conclusions
Anderson localization of electrons with more than three orders of magnitude higher density than that expected from the Mott criterion was induced by intrinsic anion disorder in perovskite oxynitride SrNbO$_2$N. The formation of a small Coulomb gap encapsulated in the localized state resulted in temperature-dependent multiple crossovers of the conduction mechanisms. The localized electron showed large magnetoresistance, which reflected the topology of the wave functions constructing the conduction band bottom split by a small lattice strain. Such
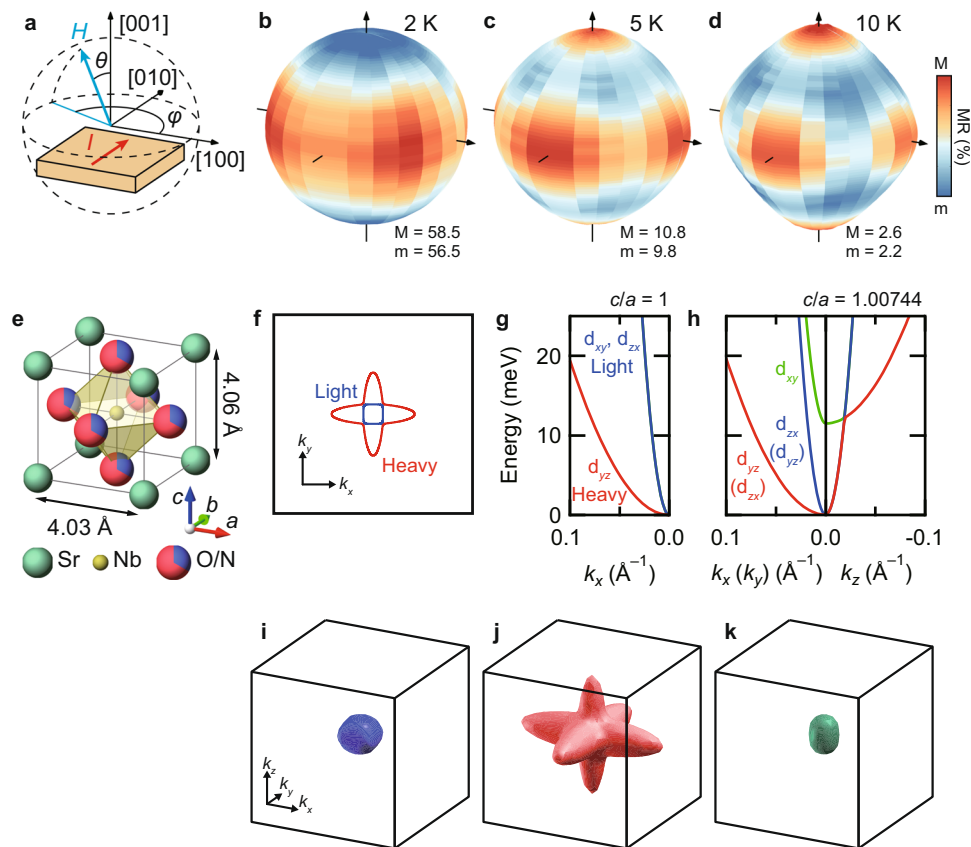
**Fig. 4 Spatial distribution of magnetoresistance and wave functions in SrNbO₂N. a** Measurement geometry on the angle dependence of magnetoresistance (MR), where $I$ and $H$ indicate electrical current and magnetic field, respectively. **b–d** Three-dimensional mapping of MR as a function of angles $\theta$ and $\varphi$ for the $SrNbO_2N$ epitaxial thin film measured under 9 T at **b** 2 K, **c** 5 K, and **d** 10 K. Both radius and colour represent the amplitude of MR. **e** Unit cell of the tetragonally distorted $SrNbO_2N$ drawn with the angle corresponding to **a**. **f, g** Band structures of cubic $SrTiO_3$ model, where **f** shows the constant energy surfaces at 50 meV higher than the bottom of the conduction band for the light- and heavy-mass bands. **h** Band structure of tetragonally distorted $SrTiO_3$ model with the same $c/a$ ratio as the experimentally observed $SrNbO_2N$ unit shown in **e**. The square frame indicates the first Brillouin zone in **f–h**. **i–k** Three-dimensional mapping of constant energy surface at 25 meV higher than the conduction band minimum for the **i** blue, **j** red, and **k** green bands in the band structure shown in **h**. The cubic frame indicates the first Brillouin zone shortened to 30% on each axis in **i–k**.

intrinsic disorder free from lattice defects is beneficial for not only experimental control of the random potential but also a theoretical investigation on localization phenomena, as indicated by the good correspondence between the anisotropy in the MR and the first-principles calculations. Thus, the present study contributes to a better understanding of electron localization and paves a way for electronic phase control by using the degree of localization as a variable parameter.

## Methods

**Film growth and characterization.** $SrNbO_{3-x}N_x$ thin films were synthesized on KTaO₃ (001) substrates ($a = 3.989$ Å; MTI corporation) at the substrate temperature of 630 °C by the nitrogen-plasma-assisted pulsed laser deposition method[18]. We controlled the nitrogen content $x$ in the films with the operation current of the electron cyclotron resonator (Tectra, Gen2) to generate nitrogen plasma. Nuclear reaction analysis was conducted to evaluate the nitrogen content $x$ in the films by using the $^{15}N(p,\alpha\gamma)^{12}C$ resonance reaction at 898 keV in a 1 MV tandetron accelerator at Tandem Accelerator Complex, University of Tsukuba. A perovskite-type crystal structure without any impurity was confirmed by X-ray diffraction using a four-axis diffractometer (Bruker AXS, d8 discover). Surface morphology was observed by an atomic force microscope (SII NanoTechnology, SPI4000 with SPA400). Resistivity $\rho$, carrier density $n$, and Hall mobility $\mu$ of the films were examined by the conventional 4-probes method and Hall effect measurements with silver electrodes using a Physical Property Measurement System (Quantum Design, PPMS Model 6000).

**Computational calculation.** We conducted the first-principles calculation based on density functional theory to elucidate the band structure of $SrTiO_3$ using the all-electron full-potential linearized augmented plane-wave + local orbitals approach

implemented in the WIEN2k software package[57,58]. We employed cubic and tetragonal unit cells with space groups of $Pm3m$ and $P4/mmm$ with relative atomic positions of Sr (0.5, 0.5, 0.5), Ti (0, 0, 0), and O (0.5, 0, 0), (0, 0.5, 0) and (0, 0, 0.5) for non-strained and strained structures, whose lattice parameters were optimized to be $a = 3.9458$ Å, and $a = 3.937$ Å and $c = 3.966$ Å, respectively, under the constant $c/a$ ratio. We used $R_{MT} \times K_{max} = 7.0$ and muffin-tin radii of 2.5, 1.96, and 1.74 a.u. for Sr, Ti, and O, respectively. Band energies were obtained on a 10,000 $k$-point mesh, using the Perdew-Burke-Ernzerhof generalized gradient approximation. The constant energy surfaces were depicted with the XCrySDen software package[59].

## Data availability

All relevant data are available from the corresponding author upon reasonable request.

## References

1. Anderson, P. W. Absence of diffusion in certain random lattices. *Phys. Rev.* **109**, 1492–1505 (1958).
2. Lee, P. A. & Ramakrishnan, T. V. Disordered electronic systems. *Rev. Mod. Phys.* **57**, 287–337 (1985).
3. Kramer, B. & MacKinnon, A. Localization: theory and experiment. *Rep. Prog. Phys.* **56**, 1469–1564 (1993).
4. Evers, F. & Mirlin, A. D. Anderson transitions. *Rev. Mod. Phys.* **80**, 1355–1417 (2008).

5. Schnyder, A. P., Ryu, S., Furusaki, A. & Ludwig, A. W. W. Classification of topological insulators and superconductors in three spatial dimensions. *Phys. Rev. B Condens. Matter Mater. Phys.* **78**, 1–22 (2008).

6. Burmistrov, I. S., Gornyi, I. V. & Mirlin, A. D. Enhancement of the critical temperature of superconductors by Anderson localization. *Phys. Rev. Lett.* **108**, 017002 (2012).

7. Li, J., Chu, R.-L., Jain, J. K. & Shen, S.-Q. Topological Anderson insulator. *Phys. Rev. Lett.* **102**, 136806 (2009).

8. Meier, E. J. et al. Observation of the topological Anderson insulator in disordered atomic wires. *Science* **362**, 929–933 (2018).

9. Stützer, S. et al. Photonic topological Anderson insulators. *Nature* **560**, 461–465 (2018).

10. Richardella, A. et al. Visualizing critical correlations near the metal-insulator transition in $Ga_{1-x}Mn_xAs$. *Science* **327**, 665–669 (2010).

11. Dobrowolska, M. et al. Controlling the Curie temperature in (Ga,Mn)As through location of the Fermi level within the impurity band. *Nat. Mater.* **11**, 444–449 (2012).

12. Mott, N. F. On the transition to metallic conduction in semiconductors. *Can. J. Phys.* **34**, 1356–1368 (1956).

13. Edwards, P. P. & Sienko, M. J. Universality aspects of the metal-nonmetal transition in condensed media. *Phys. Rev. B* **17**, 2575–2581 (1978).

14. Siegrist, T. et al. Disorder-induced localization in crystalline phase-change materials. *Nat. Mater.* **10**, 202–208 (2011).

15. Ying, T. et al. Anderson localization of electrons in single crystals: $Li_xFe_7Se_8$. *Sci. Adv.* **2**, e1501283 (2016).

16. Yang, M. et al. Anion order in perovskite oxynitrides. *Nat. Chem.* **3**, 47–52 (2011).

17. Attfield, J. P. Principles and applications of anion order in solid oxynitrides. *Cryst. Growth Des.* **13**, 4623–4629 (2013).

18. Oka, D. et al. Anion-substitution-induced nonrigid variation of band structure in $SrNbO_{3-x}N_x$ ($0 \le x \le 1$) epitaxial thin films. *ACS Appl. Mater. Interfaces* **10**, 35008–35015 (2018).

19. Oka, D., Hirose, Y., Fukumura, T. & Hasegawa, T. Heteroepitaxial growth of Perovskite $CaTaO_2N$ thin films by nitrogen plasma-assisted pulsed laser deposition. *Cryst. Growth Des.* **14**, 87–90 (2014).

20. Suzuki, A. et al. High-mobility electron conduction in oxynitride: anatase TaON. *Chem. Mater.* **26**, 976–981 (2014).

21. Oka, D. et al. Possible ferroelectricity in perovskite oxynitride $SrTaO_2N$ epitaxial thin films. *Sci. Rep.* **4**, 4987 (2015).

22. Takahashi, J. et al. Composition-induced structural, electrical, and magnetic phase transitions in $AX$-type mixed-valence cobalt oxynitride epitaxial thin films. *Appl. Phys. Lett.* **107**, 231906 (2015).

23. Sano, M., Hirose, Y., Nakao, S. & Hasegawa, T. Strong carrier localization in 3d transition metal oxynitride $LaVO_{3-x}N_x$ epitaxial thin films. *J. Mater. Chem. C* **5**, 1798–1802 (2017).

24. Oka, D. et al. Strain engineering for anion arrangement in perovskite oxynitrides. *ACS Nano* **11**, 3860–3866 (2017).

25. Oka, D., Hirose, Y., Nakao, S., Fukumura, T. & Hasegawa, T. Intrinsic high electrical conductivity of stoichiometric $SrNbO_3$ epitaxial thin films. *Phys. Rev. B* **92**, 205102 (2015).

26. Park, Y. et al. $SrNbO_3$ as a transparent conductor in the visible and ultraviolet spectra. *Commun. Phys.* **3**, 102 (2020).

27. Gunnarsson, O., Calandra, M. & Han, J. E. Colloquium: saturation of electrical resistivity. *Rev. Mod. Phys.* **75**, 1085–1099 (2003).

28. Gurvitch, M. Ioffe-Regel criterion and resistivity of metals. *Phys. Rev. B* **24**, 7404–7407 (1981).

29. Graham, M. R., Adkins, C. J., Behar, H. & Rosenbaum, R. Experimental study of the Ioffe-Regel criterion for amorphous indium oxide films. *J. Phys. Condens. Matter* **10**, 809–819 (1998).

30. Möbius, A. The metal-insulator transition in disordered solids: how theoretical prejudices influence its characterization A critical review of analyses of experimental data. *Crit. Rev. Solid State Mater. Sci.* **44**, 1–55 (2019).

31. Al'Tshuler, B. & Aronov, A. Contribution to the theory of disordered metals in strongly doped semiconductors. *Sov. J. Exp. Theor. Phys.* **50**, 968–976 (1979).

32. Möbius, A. Comment on "Critical behavior of the zero-temperature conductivity in compensated silicon, Si:(P,B)". *Phys. Rev. B* **40**, 4194–4195 (1989).

33. Shklovskiĭ, B. I. & Ėfros, A. L. *Electronic Properties of Doped Semiconductors*. (Springer, 1984).

34. Zabrodskii, A. G. & Zinov'eva, K. N. Low-temperature conductivity and metal-insulator transition in compensate $n$-Ge. *J. Exp. Theor. Phys.* **86**, 727–742 (1984).

35. Aharony, A., Zhang, Y. & Sarachik, M. P. Universal crossover in variable range hopping with Coulomb interactions. *Phys. Rev. Lett.* **68**, 3900–3903 (1992).

36. Meir, Y. Universal crossover between Efros-Shklovskii and Mott variable-range-hopping regimes. *Phys. Rev. Lett.* **77**, 5265–5267 (1996).

37. Rosenbaum, R., Lien, N. V., Graham, M. R. & Witcomb, M. A useful Mott–Efros–Shklovskii resistivity crossover formulation for three-dimensional films. *J. Phys. Condens. Matter* **9**, 6247–6256 (1997).

38. Lien, N. V. & Rosenbaum, R. General crossovers from two-dimensional Mott to soft-gap variable-range hopping. *Phys. Rev. B* **56**, 14960–14963 (1997).

39. Rosenbaum, R., Murphy, T., Palm, E., Hannahs, S. & Brandt, B. Magnetoresistance of insulating amorphous $Ni_xSi_{1-x}$ films exhibiting Mott variable-range hopping laws. *Phys. Rev. B* **63**, 094426 (2001).

40. Xu, Y., Ephron, D. & Beasley, M. R. Directed inelastic hopping of electrons through metal-insulator-metal tunnel junctions. *Phys. Rev. B* **52**, 2843–2859 (1995).

41. Wu, H. Y., Wang, W. & Lu, W. J. Temperature-dependent electrical transport mechanism in amorphous $Ge_2Sb_2Te_5$ films. *Phys. Status Solidi Basic Res.* **253**, 1855–1860 (2016).

42. Halbo, L. & Sladek, R. J. Magnetoresistance of undoped $n$-type gallium arsenide at low temperatures. *Phys. Rev.* **173**, 794–802 (1968).

43. Mansfield, R. & Kusztelan, L. Magnetoresistance and Hall effect in n-type indium antimonide in the magnetic freeze-out region. *J. Phys. C Solid State Phys.* **11**, 4157–4169 (1978).

44. Tokumoto, H., Mansfield, R. & Lea, M. J. Hopping conduction in n-type indium antimonide below 1 k. *Philos. Mag. B Phys. Condens. Matter Stat. Mech. Electron. Opt. Magn. Prop.* **46**, 93–113 (1982).

45. Schoepe, W. Variable-range hopping conduction in doped germanium at very low temperatures and high magnetic fields. *Zeitschrift für Phys. B Condens. Matter* **71**, 455–463 (1988).

46. Rosenbaum, R., Castro, H. & Schoepe, W. Numerical calculations for large positive magnetoresistance ratios $R(B)/R(0)$ in insulating materials. *Phys. B Condens. Matter* **294–295**, 486–488 (2001).

47. Rosenbaum, T. F. et al. Metal-insulator transition in a doped semiconductor. *Phys. Rev. B* **27**, 7509–7523 (1983).

48. Ebbinghaus, S. G. et al. Perovskite-related oxynitrides—recent developments in synthesis, characterisation and investigations of physical properties. *Prog. Solid State Chem.* **37**, 173–205 (2009).

49. Nanamatsu, S., Kimura, M. & Kawamura, T. Crystallographic and dielectric properties of ferroelectric $A_2B_2O_7$ (A=Sr, B=Ta, Nb) crystals and their solid solutions. *J. Phys. Soc. Jpn.* **38**, 817–824 (1975).

50. Kikuchi, R., Nakamura, T., Tamura, S., Kaneko, Y. & Hato, K. Fundamental semiconducting properties of perovskite oxynitride $SrNbO_2N$: epitaxial growth and characterization. *Chem. Mater.* **29**, 7697–7703 (2017).

51. Schwartz, T., Bartal, G., Fishman, S. & Segev, M. Transport and Anderson localization in disordered two-dimensional photonic lattices. *Nature* **446**, 52–55 (2007).

52. Esat Kondakci, H., Abouraddy, A. F. & Saleh, B. E. A. Discrete Anderson speckle. *Optica* **2**, 201–209 (2015).

53. Hinuma, Y. et al. First-principles study on relaxor-type ferroelectric behavior without chemical inhomogeneity in $BaTaO_2N$ and $SrTaO_2N$. *Chem. Mater.* **24**, 4343–4349 (2012).

54. Mattheiss, L. F. Energy bands for $KNiF_3$, $SrTiO_3$, $KMoO_3$, and $KTaO_3$. *Phys. Rev. B* **6**, 4718–4740 (1972).

55. Rödel, T. C. et al. Two-dimensional electron systems in $ATiO_3$ perovskites (A = Ca, Ba, Sr): control of orbital hybridization and energy order. *Phys. Rev. B* **96**, 041121 (2017).

56. Uwe, H., Kinoshita, J., Yoshihiro, K., Yamanouchi, C. & Sakudo, T. Evidence for light and heavy conduction electrons at the zone center in $KTaO_3$. *Phys. Rev. B* **19**, 3041–3044 (1979).

57. Schwarz, K. & Blaha, P. Solid state calculations using WIEN2k. *Comput. Mater. Sci.* **28**, 259–273 (2003).

58. Blaha, P. et al. WIEN2k: An APW+lo program for calculating the properties of solids. *J. Chem. Phys.* **152**, 074101 (2020).

59. Kokalj, A. XCrySDen—a new program for displaying crystalline structures and electron densities. *J. Mol. Graph. Model.* **17**, 176–179 (1999).

## Acknowledgements

## Author contributions

D.O. and Y.H. conceived the idea and designed the study under the supervision of T.H. D.O. performed the film growth, electrical measurements, data analyses, and first-principles calculations with assistance from Y.H., S.N., T.F., and T.H. All authors contributed to write the article.

## Competing interests

The authors declare no competing interests.

**Additional information**

**Supplementary information** The online version contains supplementary material available at https://doi.org/10.1038/s42005-021-00777-z.

**Correspondence** and requests for materials should be addressed to Daichi Oka.

**Peer review information** *Communications Physics* thanks the anonymous reviewers for their contribution to the peer review of this work.

**Reprints and permission information** is available at http://www.nature.com/reprints

**Publisher's note** Springer Nature remains neutral with regard to jurisdictional claims in published maps and institutional affiliations.